A&A 532, A127 (2011)
DOI: 10.1051/0004-6361/201116506

Astronomy & Astrophysics

A H_2CO and H110α survey of H II regions with the 25-m radio telescope of Nanshan Station⋆

Z. M. Du[1,2], J. J. Zhou[1,3], J. Esimbek[1,3], X. H. Han[1,2], and C. P. Zhang[1,2]

[1] Xinjiang Astronomical Observatory, Chinese Academy of Sciences, Urumqi 830011, PR China
e-mail: zhimaodu@gmail.com
[2] Graduate University of the Chinese Academy of Sciences, Beijing 100080, PR China
[3] Key Laboratory of Radio Astronomy, Chinese Academy of Sciences, Urumqi 830011, PR China

Received 13 January 2011 / Accepted 6 June 2011

ABSTRACT

Context. Accurate distances are necessary for determining the physical properties of massive star-formation regions and the structure of our Galaxy. One way to approach these studies is by determining the kinematic distances of H II regions.
Aims. This study determines the kinematic distances of H II regions located in the inner Galaxy and studies their spatial distribution.
Methods. We observed 251 H II regions with the 25-m radio telescope of Nanshan Station, looking for H_2CO absorption lines and H110α radio recombination lines (RRLs). The kinematic distances were calculated using the velocity of H110α lines and a model of the Galactic rotation. The kinematic distance ambiguity was resolved using the H_2CO velocities.
Results. We detected the H110α RRLs in 28 sources and H_2CO absorption lines in 59 sources. In the latter case, 43 features had not previously been observed. H_2CO and H110α lines were simultaneously detected toward 23 H II regions. We resolved the kinematic distance ambiguities for 14 H II regions and 20 intervening molecular clouds.
Conclusions. Our statistical analysis shows that UCH II regions are tightly confined to the Galactic plane, and their vertical height distribution is about 25.4 pc. The corresponding value of the H II regions is 28.6 pc. There is a good statistical relationship between the fluxes of H_2CO and infrared 100 μm, for those H II regions with both H_2CO absorption lines and H110α RRLs detected. This suggests that there is a weak correlation between the continuum fluxes at 6 cm and infrared 100 μm.

Key words. Galaxy: structure – H II regions – ISM: molecules – radio lines: ISM

1. Introduction

Young massive stars and their H II regions are good tracers of the spiral structure of the Galaxy (Churchwell 2002). Their distances are therefore fundamentally important to outline the spiral structure of our own Galaxy. Accurate distance measurements are also needed to constrain the physical properties of H II regions such as size, bolometric luminosity, and mass. However, optical methods of distance measurement are very difficult to apply because H II regions are heavily obscured by interstellar dust. An alternative approach is to calculate the kinematic distances of H II regions based on radio emission, which is not attenuated by intervening dust, such as recombination lines or molecular lines.

Kinematic distances are calculated using measured radial velocities and the rotation model of the Galaxy, if the H II region is located in the outer Galaxy (outside the solar circle). However, if the H II region is located in the inner Galaxy (inside the solar circle), there are two possible interpretations of the data. Our line of sight typically intersects the circular orbit of the H II region at two points, called the near and far distances. The object has the same radial velocity at both points on its orbit, therefore, we cannot uniquely determine the location of an H II region in the inner galaxy with radial velocity data alone. This degeneracy is referred to as the kinematic distance ambiguity (KDA). Only sources located at a tangent point will have unambiguous distances (Sewilo et al. 2004).

The method of employing H_2CO absorption lines to resolve the KDA was first used by Wilson (1972). Downes et al. (1980) resolved the KDAs of 262 H II regions by observing H_2CO absorption lines with the Effelsberg 100-m telescope. More recently, Araya et al. (2002), Watson et al. (2003), and Sewilo et al. (2004) used H_2CO absorption lines to resolve the KDAs of 109 sources using the 305 m Arecibo telescope and the NRAO Green Bank Telescope (GBT), respectively. Other spectral lines can be used to find the correct kinematic distance, Kolpak et al. (2003) and Fish et al. (2003) used the Very Large Array (VLA) to observe the 21 cm H I absorption spectrum and successfully obtained the kinematic distances of 49 and 20 H II regions. Anderson & Bania (2009) resolved KDAs of 266 H II regions using existing HI and ^{13}CO survey data.

Compared with the distance derived from trigonometric parallaxes of massive star-formation regions, the errors of kinematic distance are larger. But determining kinematic distance is relatively easy, it is still widely used by many authors in recent years (Anderson & Bania 2009; Hou et al. 2009).

Continuing this tradition of research on the structure of our Galaxy, our study determines kinematic distances to more H II regions. We have measured H_2CO absorption lines and H110α radio recombination lines (RRLs) for 251 H II regions. Section 2 describes our sample selection criteria and observations. Section 3 describes our data reduction procedure and presents the distribution of H II regions perpendicular to the Galactic Plane. In Sect. 4 we discuss the relationship between the flux of H_2CO and infrared 100 μm flux density. Section 5 contains a brief summary of the paper and our conclusions.

⋆ Figures 1–3 and Tables 1–4 are available in electronic form via http://www.aanda.org

2. Observations

2.1. Sample

We selected 120 sources from the IRAS Point Source catalog that satisfy the color-color criteria for UCH II regions: $\log(S_{60\,\mu m}/S_{12\,\mu m}) \geq 1.30$ and $\log(S_{25\,\mu m}/S_{12\,\mu m}) \geq 0.57$ (Wood & Churchwell 1989). Sixty-one sources were selected from Quireza et al. (2006) and 70 sources were selected from Lockman (1989). In addition, we required all candidate sources to be visible with the 25-m radio telescope and lie in the galactic latitude range $\geq -30°$. Some sources of the sample are located in the outer Galaxy to use our allotted observation time efficiently.

2.2. Observations

Our observations were conducted from September 2009 to August 2010 with the 25-m radio telescope located at Nanshan station (87° E, 43° N, altitude 2080 m) of the Xinjiang Astronomical Observatory of the Chinese Academy of Sciences. The λ 6 cm receiving system was constructed at the Max-Planck-Institut für Radioastronomie (MPIfR) in Germany and installed at the telescope in August 2004. Its half power beam width (HPBW) at 4.86 GHz is 9.5′. One digital autocorrelation spectrometer with 4096 channels was installed on the back-end, the maximum bandwidth of the spectrometer is 80 MHz. The *C*-band cryogenic receiver system temperature was maintained at 23 K during the observation. The pointing accuracy was 15″ in all observations and the main beam efficiency was 65%.

We observed the H_2CO absorption line (ν_0 = 4829.6594 MHz) and the H110α RRL (ν_0 = 4874.1570 MHz) simultaneously with 4940 km s^{-1} bandwidth, corresponding to a spectral resolution of 1.206 km s^{-1}. Position-switching mode was adopted. A noise-diode calibration signal was used to calibrate the spectrum. The flux error was ∼15%; the degrees-per-flux-unit value was 0.116 K Jy^{-1} at 6cm wavelength. To observe more sources during the allotted observation time, we observed every source with 6 min integration time at first. We observed those sources with a signal (H110α RRLs or H_2CO absorption lines) continuously until we attained a signal-to-noise ratio (S/N) > 3. We discarded sources without a signal. The rms for 6 min integration time lies in the range of 0.23 ∼ 0.47 Jy, and the actual value mainly depends on weather and elevation.

All sources were observed in "broad band mode" and the center frequency was 4800 MHz with a bandwidth 600 MHz. The flux densities were determined with a "cross-scans" approach. Every cross-scan includes eight individual subscans. half of the eight subscans were performed in azimuth and the other four in elevation. A Gaussian distribution was fitted to every subscan. By using frequently observed primary calibrators such as 3C 286, 3C 48, 0951+699, and NGC 7027, we integrated our observations into the absolute flux density scale (Baars et al. 1977; Ott et al. 1994). The flux densities of 6 cm continuum are listed in Col. 6 of Table 1.

3. Results

The H110α and H_2CO absorption line parameters were derived from Gaussian fits using the CLASS software package. The sources with H_2CO absorption lines or H110α RRLs or both are listed in Table 1. The fit results for H110α and H_2CO lines are presented in Table 2 and Table 3, respectively. The errors quoted in the tables are the formal 1σ errors of the Gaussian fits. Figure 1 displays the H_2CO spectra of those H II regions for which only H_2CO absorption lines were detected. The H_2CO absorption feature of IRAS 17432-2835 has a larger line width, while the NH3 (1, 1) line width of the source is about 40 km s^{-1} (Hüttemeister et al. 1993), which is consistent with IRAS 17432-2835 ′s location in the Galactic center (Miyazaki & Tsuboi 2000). Figure 2 displays the H110α spectra of those H II regions for which only H110α RRLs was detected. Sources for which both lines were detected are displayed in Fig. 3.

Among 251 H II regions observed in this survey, 28 had H110α RRLs and 59 had H_2CO absorption lines. For 43 of the regions, this work represents the first such detection. Both H_2CO and H110α lines were detected toward 23 H II regions, 9 of which were previously observed by Downes et al. (1980, see Table 1). In addition, IRAS 23116+6111 was reported by Reid et al. (2009).

3.1. Kinematic distance calculation

All kinematic distances were calculated using the Galaxy rotation curve of Reid et al. (2009), with parameters R_0 = 8.4 kpc, and Θ_0 = 254 km s^{-1}.

In Table 4 we report the kinematic parameters of 16 H II regions and 20 intervening molecular clouds. These parameters are the radial velocity of the sources (V_{LSR}), the near (D_{near}) and far (D_{far}) distances, the velocity of the tangent point (V_{TP}), the distance to the tangent point (D_{TP}), the kinematic distance measure selected as best representing the distance to the source (D_{LSR}), the distance from the Galactic plane (z), and the distance to the Galactic center (R_{GC}). We followed the method of Reid et al. (2009), and calculated the errors of the kinematic distances assuming an LSR velocity uncertainty of 7 km s^{-1}. It should be noted that the beam of the Nanshan Station 25-m radio telescope is very large and has the higher probability to detect H II region and H_2CO molecular cloud in the same beam, but they may actually not lie on the same line of sight. This is especially true when we observed the crowded regions of the inner Galaxy.

To determine kinematic distances, we made the following assumptions. (1) The H_2CO absorption lines are produced by clouds that lie in the Galactic disk between us and the H II regions; (2) the entire H_2CO absorption lines can be explained by the absorption of a thermal bremsstrahlung radio continuum from a single background H II region. In other words, we assumed that only one H II region is located within the beam.

We were able to resolve the KDA for 14 H II regions and 20 intervening H_2CO molecular clouds following the method of Sewilo et al. (2004). Two of the H II regions are assigned to the far distance, eight are assigned at the near distance, and four are placed at the tangent point (see Table 4). For the remaining five sources, we were unable to distinguish between the near and far distances because they do not fit our classification. Among the intervening H_2CO molecular clouds, three are at the tangent point, two is at the near distance, one are unclassified and one does not have assigned distances. The other fifteen molecular clouds are associated with H II regions: eight at the near distance, one at the far distance and two at the tangent point, four are associated with H II region. The last two are associated with H II region IRAS 23116+6111 (NGC 7538) and IRAS 06053-0622 (Mon R2), which have an unambiguous distance, because they lie outside the solar circle.

The sources near longitude 0° or 180° have radial velocities that are dominated by peculiar motions rather than circular velocities (Sewilo et al. 2004; Gómez 2006). The kinematic distances derived from this radial velocity will have large error.

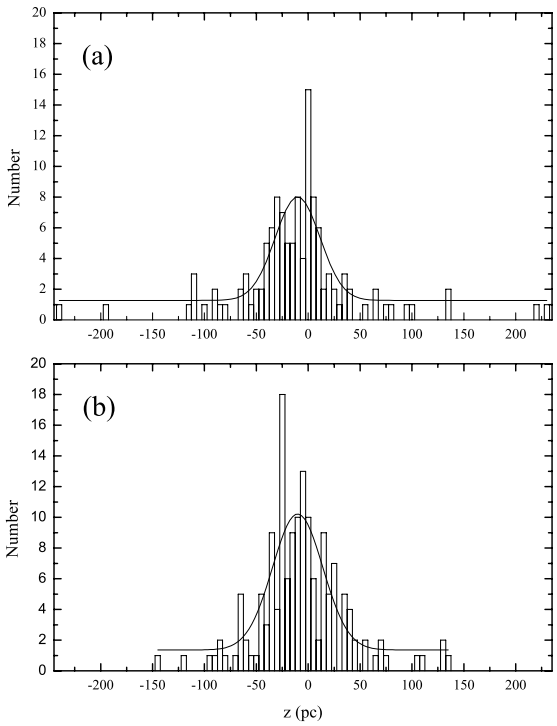

Fig. 4. Panel **a)** is the histogram of the vertical height of 121 H II regions (including 109 UCH II regions) with respect to the Galactic plane, the half width at half maximum is 25.4 ± 7.1 pc. Panel **b)** is the histogram of the vertical height of 157 H II regions from Boston university H II region catalog, the half width at half maximum is 28.6 ± 8.7 pc. Positive height corresponds to positive Galactic latitude. The overlaid curve shows the Gaussian fit to the data.

G1.13-0.1 and IRAS 17441-2822 (Sgr B2) are near the Galactic center and their kinematic distances are uncertain. Kinematic parameters of these two sources were not listed in Table 4.

3.2. Vertical height distribution of H II regions

Figure 4a shows the vertical height distribution of the 121 sources (109 UCH II regions and 12 H II regions) above and below the Galactic plane that are taken from this survey and some similar studies (Araya et al. 2002; Watson et al. 2003; Sewilo et al. 2004; Han et al. 2011). The Gaussian fit has a half width at half maximum (*HWHM*) of 25.4 ± 7.1 pc and is centered at −10.2 ± 3.0 pc. Because 109 sources of this group are UCH II regions, this indicates that UCH II are tightly confined to the Galactic plane and that the thickness of the star-forming layer is about 25.4 pc. Figure 4b shows the vertical height distribution of the 157 H II regions are perpendicular to the Galactic plane, and these sources are taken from the Boston University H II Region Catalog (Anderson & Bania 2009). The *HWHM* is 28.6 ± 8.7 pc and the central value is −10.2 ± 3.5 pc. This difference is probably caused by the uncertainty of distance measurement. Evidently, a much larger sample of H II regions with determined distance is needed before we can achieve accurate thickness of H II regions perpendicular to the Galactic plane.

We found that more sources lie below the Galactic plane than above the Galactic plane and the distribution of H II regions centered at −10.2 ± 3.0 pc. This bias could arise because we defined a Galactic plane centered on the Sun, parallel to, but offset by 8 pc from the symmetry plane of the Galaxy. A similar bias was obtained by Fish et al. (2003), who found the distribution of H II regions to be centered at −7.3 ± 1.4 pc.

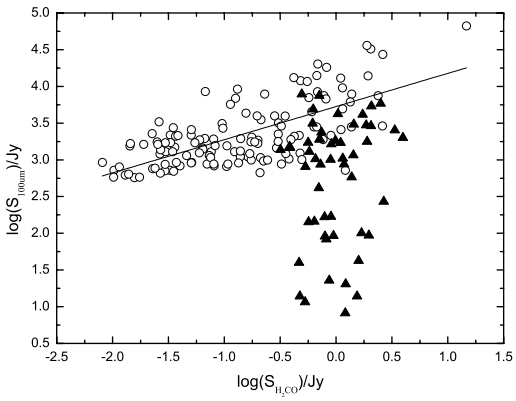

Fig. 5. Relationship between $\log(S_{H_2CO})$ and $\log(S_{100\,\mu m})$, the circles represent the sources detected in H110α RRLs, and solid triangles represent the sources not detected in H110α RRLs.

4. Discussions

Figure 5 shows the relationship between the flux of H_2CO and the infrared 100 μm flux density of UCH II regions. For these two quantities, 137 sources were collected from the literature (Watson et al. 2003; Sewilo et al. 2004; Han et al. 2011), and 51 sources were taken from our own data. There clearly are a horizontal branch and a vertical branch in the figure.

The horizontal branch contains those sources with H110α RRLs and H_2CO absorption lines. It shows that $\log(S_{H_2CO})$ is linearly correlated with $\log(S_{100\,\mu m})$: $\log(S_{100\,\mu m}) = (3.73 \pm 0.04) + (0.45 \pm 0.04) \times \log(S_{H_2CO})$ (where the flux of H_2CO is expressed as its absolute value), and the correlation coefficient of this branch is 0.65. We know that the flux of H_2CO is mainly determined by 6cm continuum emission of the background source (Downes et al. 1980). Therefore, the relation above indicates that there is a correlation between the continuum fluxes at 6 cm and infrared 100 μm. Even if the H II region and H_2CO molecular clouds are not in close contact, this conclusion is valid.

The vertical branch has a weak correlation, and the correlation coefficient is 0.23. All 52 sources belonging to this branch come from our sample and Han et al. (2011). Sources of this group were not detected in H110α RRLs. The 6 cm continuum emission was detected toward all these sources except for IRAS 03271+3013, IRAS 18048-2131, and IRAS 20332+4124. Maybe those three sources are too weak to be detected by our telescope. The 6 cm continuum emissions of the sources in the vertical branch are weak, corresponding main beam brightness temperatures are usually less than 1–2 K. In this case, some other mechanism may work and affect the H_2CO flux, while the 6cm continuum flux is not proportional to H_2CO absolute flux.

5. Summary and conclusions

Using the Nanshan Station 25-m radio telescope of Xinjiang Astronomical Observatory, we have observed the H_2CO absorption lines and H110α RRLs toward 251 H II regions. We detected H110α RRLs in 28 sources and H_2CO absorption lines in 59 sources, among which 43 H_2CO sources had not previously been detected. H_2CO and H110α lines were simultaneously detected toward 23 H II regions, 9 of which had been detected by Downes et al. (1980) and one of which (IRAS 23116+6111) had been reported by Reid et al. (2009). The detection rate of H_2CO absorption lines in our survey is 23.5%.

Based on the method of Sewilo et al. (2004) and a modified Galactic rotation curve, we resolved the KDAs for 14 observed H II regions and 20 intervening molecular clouds. The thickness of vertical height distribution of UCH II regions perpendicular to the Galactic plane was found to be 25.4 ± 7.1 pc within the solar circle.

We find that there is a strong correlation between the H_2CO flux and the infrared 100 μm flux density of H II regions, $\log(S_{100\mu m}) = (3.73 \pm 0.04) + (0.45 \pm 0.04) \times \log(S_{H_2CO})$. This relation suggests that there is a correlation between the continuum fluxes at 6 cm and infrared 100 μm. Those sources without H110α features only show strong H_2CO absorption lines. Their 6cm continuum fluxes are weak, some mechanism different from collision may be at work even though the 6cm continuum flux is not proportional to the H_2CO absolute flux.

Acknowledgements. We thank Dr. Mark Reid for providing us the Fortran code for the estimation of kinematic distances. We also are very grateful to Jun Liu for processing the 6cm continuum data. This work was funded by The National Natural Science foundation of China under grant 10873025 and 10778703, and by The Program of the Light in China's Western Region (LCRW) under grant No. RCPY200605 and RCPY200706.

References

Anderson, L. D., & Bania, T. M. 2009, ApJ, 690, 706
Araya, E., Hofner, P., Churchwell, E., & Kurtz, S. 2002, ApJS, 138, 63
Araya, E., Hofner, P., Linz, H., et al. 2004, ApJS, 154, 579
Baars, J. W. M., Genzel, R., Pauliny-Toth, I. I. K., & Witzel, A. 1977, A&A, 61, 99
Churchwell, E. 2002, ARA&A, 40, 27
Downes, D., Wilson, T. L., Bieging, J., & Wink, J. 1980, A&AS, 40, 379
Fish, V. L., Reid, M. J., Wilner, D. J., & Churchwell, E. 2003, ApJ, 587, 701
Gómez, G. C. 2006, AJ, 132, 2376
Han, X. H., Zhou, J. J., Esimbek, J., Wu, G., & Gao, M. F. 2011, Res. Astron. Astrophys., 11, 156
Hou, L. G., Han, J. L., & Shi, W. B. 2009, A&A, 499, 473
Hüttemeister, S., Wilson, T. L., Bania, T. M., & Martín-Pintado, J. 1993, A&A, 280, 255
Kolpak, M. A., Jackson, J. M., Bania, T. M., Clemens, D. P., & Dickey, J. M. 2003, ApJ, 582, 756
Lockman, F. J. 1989, ApJS, 71, 469
Miyazaki, A., & Tsuboi, M. 2000, ApJ, 536, 357
Ott, M., Witzel, A., Quirrenbach, A., et al. 1994, A&A, 284, 331
Quireza, C., Rood, R. T., Balser, D. S., & Bania, T. M. 2006, ApJS, 165, 338
Reid, M. J., Menten, K. M., Zheng, X. W., et al. 2009, ApJ, 700, 137
Sewilo, M., Watson, C., Araya, E., et al. 2004, ApJS, 154, 553
Watson, C., Araya, E., Sewilo, M., et al. 2003, ApJ, 587, 714
Whiteoak, J. B., & Gardner, F. F. 1974, A&A, 37, 389
Wilson, T. L. 1972, A&A, 19, 354
Wood, D. O. S., & Churchwell, E. 1989, ApJ, 340, 265

Pages 5 to 13 are available in the electronic edition of the journal at http://www.aanda.org

Table 1. The sources with H_2CO absorption lines or H110α RRLs or both of them.

Source	Name	RA(2000) (^{h} ^{m} ^{s})	Dec(2000) ($^\circ$ $'$ $''$)	Rms[a] (Jy)	$S_{100\ \mu m}$ (10^3Jy)	$S_{6\ cm}$[b] (Jy)	Note
IRAS 01202+6133		01 23 32.33	+61 48 48.7	0.124	1.72	0.90	
IRAS 03271+3013		03 30 14.90	+30 23 48.5	0.125	0.01	...	
IRAS 05375−0731	S235	05 39 56.06	−07 30 26.1	0.157	0.27	6.77	
IRAS 05379+3550		05 41 20.53	+35 52 06.8	0.119	1.47	2.39	
IRAS 05450+0019		05 47 34.62	+00 20 07.9	0.197	0.10	0.29	
IRAS 05454+0034		05 47 59.22	+00 35 31.2	0.184	0.02	0.31	
IRAS 06053−0622	Mon R2	06 07 46.67	−06 22 59.6	0.215	20.2	8.53	
IRAS 06055+2039		06 08 32.82	+20 39 16.2	0.110	1.71	1.26	
IRAS 17417−2851		17 44 53.42	−28 52 20.0	0.323	1.77	13.11	
IRAS 17418−2927		17 44 59.55	−29 28 53.6	0.189	0.87	20.78	
IRAS 17420−2902		17 45 14.80	−29 03 18.4	0.322	6.87	127.03	
IRAS 17430−2900		17 46 16.07	−29 01 37.0	0.229	2.54	204.62	
IRAS 17432−2855		17 46 26.73	−28 56 11.2	0.234	4.15	120.70	
IRAS 17432−2835		17 46 27.43	−28 36 06.1	0.243	3.03	27.29	
IRAS 17441−2822	Sgr B2	17 47 19.61	−28 23 07.3	0.237	66.7	54.63	*d,f*
IRAS 17449−2855		17 48 10.47	−28 56 55.6	0.360	2.01	12.01	*d*
G1.13−0.1		17 48 39.29	−28 01 57.5	0.181	...	10.17	
IRAS 17455−2805		17 48 42.22	−28 06 49.3	0.240	5.39	7.99	
IRAS 18035−2126		18 06 35.91	−21 26 00.7	0.194	1.05	2.58	
IRAS 18048−2131		18 07 51.72	−21 30 53.2	0.204	0.14	...	
IRAS 18060−2005	W31	18 08 58.52	−20 05 24.2	0.124	12.0	14.73	*f*
G10.159−0.34	W31 A	18 09 23.52	−20 19 13.4	0.185	...	47.73	*d*
IRAS 18064−2008		18 09 24.27	−20 08 07.4	0.242	1.16	13.40	*f*
G12.807−0.20	W33	18 14 14.88	−17 55 44.1	0.175	...	38.57	*d,f*
IRAS 18114−1718		18 14 23.26	−17 17 34.5	0.192	1.01	5.54	
IRAS 18127−1717		18 15 38.13	−17 16 29.0	0.202	0.81	4.89	
G14.626+0.08		18 16 48.35	−16 11 28.8	0.134	...	12.51	
IRAS 18141−1615	RCW 157	18 17 02.22	−16 14 38.8	0.298	2.82	12.56	*f*
G18.686+1.96	RCW 160	18 17 55.63	−11 43 36.8	0.177	...	13.26	
G15.032−0.68	M17 S	18 20 26.74	−16 11 59.9	0.351	...	376.01	
G15.181−0.62		18 20 30.64	−16 02 21.7	0.321	...	131.81	*d,f*
G15.095−0.71	M17 N	18 20 40.19	−16 09 29.0	0.366	...	328.30	
IRAS 18222−1317		18 25 02.27	−13 15 50.8	0.175	8.49	11.67	*d*
G19.608−0.23		18 27 38.05	−11 56 41.5	0.202	...	9.46	*d,f*
IRAS 18258−0737		18 28 34.15	−07 35 31.2	0.176	1.90	0.14	
IRAS 18265−1517		18 29 24.80	−15 15 48.9	0.163	1.30	0.30	
G23.421−0.21		18 34 43.95	−08 33 18.6	0.220	...	9.82	*d,f*
IRAS 18328−0735		18 35 31.17	−07 33 22.1	0.195	2.98	10.02	
IRAS 18406−0338		18 43 17.54	−03 35 45.4	0.186	3.13	4.59	
IRAS 18408−0348		18 43 31.12	−03 44 57.5	0.209	0.87	5.37	*e,f*
IRAS 18446−0150		18 47 13.96	−01 47 13.4	0.305	1.88	14.34	
G30.776−0.03	W43	18 47 36.42	−01 55 54.8	0.220	...	69.35	*d,f*
IRAS 18454−0158		18 48 01.30	−01 54 49.1	0.202	2.90	51.10	
IRAS 18461−0136		18 48 44.59	−01 33 16.0	0.091	1.52	7.11	
IRAS 18507+0110	NRAO 584	18 53 19.41	+01 14 34.7	0.179	32.5	13.72	*f*
IRAS 18530+0215		18 55 34.19	+02 19 08.3	0.129	1.92	3.35	
IRAS 18536+0753		18 56 03.75	+07 57 25.6	0.216	4.22	4.32	
G40.505+2.54	S76	18 56 12.82	+07 53 39.3	0.245	...	5.09	
IRAS 18566+0408		18 59 09.87	+04 12 13.6	0.143	1.03	3.66	*c*
IRAS 18592+0108		19 01 46.95	+01 13 07.6	0.236	14.0	15.08	
IRAS 19111+1048		19 13 27.81	+10 53 33.9	0.200	7.50	6.99	
IRAS 19120+1103		19 14 21.73	+11 09 13.7	0.121	7.89	10.96	*d,f*
IRAS 19124+1106		19 14 45.28	+11 11 58.3	0.162	0.58	6.03	
G46.495−0.25		19 17 26.49	+11 55 54.4	0.136	...	4.20	
IRAS 19181+1349		19 20 28.06	+13 55 26.0	0.138	5.23	8.50	
G48.930−0.28		19 22 26.08	+14 07 08.1	0.115	...	39.98	
G49.384−0.30		19 23 12.00	+14 27 31.2	0.149	...	41.69	
G49.582−0.38	W51	19 23 42.06	+14 30 33.3	0.191	...	99.44	*f*
IRAS 19598+3324	K3-50	20 01 45.60	+33 32 44.1	0.198	13.0	13.36	
G79.293+1.30	DR 7	20 28 09.55	+40 51 42.5	0.122	...	13.48	
G81.253+1.12		20 35 06.22	+42 20 23.6	0.214	...	14.20	
IRAS 20332+4124		20 35 00.45	+41 34 48.2	0.098	1.38	...	
IRAS 23033+5951		23 05 25.16	+60 08 11.6	0.108	1.83	1.09	
IRAS 23116+6111	NGC 7538	23 13 45.63	+61 28 17.7	0.152	14.1	20.65	

Notes. [a] The rms of the spectral lines were obtained during our observation. [b] The measurement results of the continuum flux densities at 6 cm; [c] data reported by Araya et al. (2004); [d] data reported by Downes et al. (1980); [e] data reported by Wilson (1972); [f] data reported by Whiteoak & Gardner (1974).

Table 2. H110α RRL parameters.

Source	$V_{\rm LSR}$ (km s^{-1})	*FWHM* (km s^{-1})	$S_{\rm H110\alpha}$ (Jy)	$\int S_v {\rm d}v$ (Jy km s^{-1})
G1.13−0.1	−23.43(1.23)	18.84(3.11)	0.324(0.118)	6.491(0.872)
G10.159−0.34	10.80(0.651)	34.93(1.56)	1.11(0.160)	41.12(1.57)
G12.807−0.20	35.14(0.908)	32.50(2.17)	0.737(0.151)	25.49(1.44)
G14.626+0.08	34.67(0.623)	21.82(1.91)	0.728(0.127)	16.90(1.09)
G15.032−0.687	17.72(0.608)	32.40(1.33)	3.39(0.477)	116.9(4.37)
G15.095−0.71	16.71(0.506)	36.11(1.17)	3.73(0.413)	143.2(4.07)
G15.181−0.63	17.09(0.485)	33.32(1.07)	1.63(0.179)	57.70(1.68)
G18.686+1.96	25.74(1.31)	26.33(3.27)	0.409(0.134)	11.48(1.17)
G19.608−0.23	46.49(1.82)	25.31(4.05)	0.268(0.125)	7.213(1.02)
G30.776−0.03	94.05(0.459)	31.53(1.16)	1.63(0.175)	54.74(1.66)
G46.495−0.25	55.63(0.864)	19.56(1.94)	0.264(0.067)	5.501(0.484)
G48.930−0.28	64.55(0.496)	24.73(1.21)	0.905(0.118)	23.81(0.981)
G49.384−0.30	54.46(0.748)	25.55(1.66)	0.757(0.147)	20.59(1.20)
G49.582−0.38	58.98(0.436)	30.95(0.994)	1.66(0.171)	54.69(1.56)
G79.293+1.30	−42.02(0.841)	23.06(1.89)	0.299(0.640)	7.340(0.511)
G81.253+1.123	12.71(0.802)	21.42(2.04)	0.339(0.765)	7.738(0.603)
IRAS 06053−0622	10.18(1.32)	24.24(3.26)	0.129(0.045)	3.319(0.375)
IRAS 17441−2822	59.59(1.10)	42.79(2.38)	0.452(0.099)	20.59(1.04)
IRAS 18060−2005	7.772(1.20)	29.83(2.93)	0.440(0.127)	13.98(1.16)
IRAS 18141−1615	33.78(0.795)	27.29(1.71)	0.498(0.965)	14.46(0.816)
IRAS 18222−1317	48.79(1.11)	21.58(2.54)	0.347(0.108)	7.977(0.824)
IRAS 18454−0158	98.95(0.877)	33.51(2.11)	0.807(0.160)	28.79(1.54)
IRAS 18507+0110	54.70(0.836)	23.23(2.02)	0.412(0.942)	10.20(0.755)
IRAS 18592+0108	45.59(0.969)	20.00(2.56)	0.382(0.108)	8.130(0.836)
IRAS 19181+1349	19.58(1.20)	22.52(2.52)	0.250(0.820)	5.996(0.625)
IRAS 19120+1103	56.07(1.15)	20.83(2.91)	0.317(0.106)	7.036(0.814)
IRAS 19598+3324	−23.33(1.10)	25.38(2.67)	0.306(0.873)	8.264(0.734)
IRAS 23116+6111	−59.34(1.39)	20.00(2.76)	0.379(0.156)	8.067(1.09)

Notes. Table 2 lists 28 H II regions (23 also with H_2CO absorption lines, 5 only with H110α RRLs) with H110α RRLs. The values in parentheses are the formal 1σ errors of the Gaussian fit.

Table 3. H_2CO line parameters.

Source direction[a]	$V_{\rm LSR}$ (kms^{-1})	*FWHM* (km s^{-1})	$S_{\rm H_2CO}$ (Jy)	$\int S_v {\rm d}v$ (Jy km s^{-1})
IRAS 01202+6133MC1	−11.81(0.310)	2.852(0.800)	−0.563(0.129)	−1.708(0.379)
IRAS 03271+3013MC1	8.907(0.147)	1.206(1.97)	−1.21(0.182)	−1.556(0.323)
IRAS 05375−0731MC1	5.116(0.708)	2.381(0.150)	−2.68(0.159)	−6.798(0.395)
IRAS 05379+3550MC1	−19.65(0.495)	4.598(1.11)	−0.389(0.107)	−1.904(0.384)
IRAS 05450+0019MC1	9.717(0.131)	2.065(0.284)	−1.69(0.190)	−3.707(0.461)
IRAS 05454+0034MC1	9.652(0.194)	1.907(0.369)	−1.22(0.200)	−2.469(0.458)
IRAS 06053−0622MC1	10.51(0.082)	4.581(0.164)	−1.010(0.051)	−4.930(0.172)
IRAS 06055+2039MC1	8.260(0.132)	2.948(0.340)	−1.10(0.106)	−3.458(0.315)
IRAS 17417−2851MC1	−3.654(0.346)	7.051(0.713)	−1.90(0.309)	−14.26(1.32)
IRAS 17418−2927MC1	−132.8(1.63)	38.12(4.89)	−0.568(0.194)	−23.04(2.19)
IRAS 17418−2927MC2	−56.62(0.598)	22.73(1.52)	−1.18(0.194)	−28.62(1.58)
IRAS 17418−2927MC3	−3.037(0.257)	3.980(0.555)	−1.15(0.194)	−4.864(0.621)
IRAS 17420−2902MC1	−54.12(0.289)	5.512(0.654)	−2.51(0.395)	−14.72(1.53)
IRAS 17420−2902MC2	−6.030(0.455)	9.710(1.67)	−2.08(0.395)	−21.45(4.33)
IRAS 17420−2902MC3	24.62(1.86)	56.81(4.05)	−2.09(0.395)	−126.6(7.97)
IRAS 17430−2900MC1	−53.38(0.492)	8.143(1.54)	−2.50(0.569)	−21.71(3.00)
IRAS 17430−2900MC2	−8.230(0.956)	11.73(2.87)	−1.75(0.569)	−21.85(3.67)
IRAS 17430−2900MC3	41.94(0.779)	33.16(1.77)	−3.36(0.569)	−118.5(5.43)
IRAS 17432−2835MC1	13.90(0.959)	43.25(2.00)	−1.44(0.276)	−66.29(2.89)
IRAS 17432−2855MC1	−137.0(2.00)	51.93(5.59)	−1.15(0.301)	−63.54(4.50)
IRAS 17432−2855MC2	−52.49(0.426)	7.697(0.773)	−1.48(0.301)	−12.15(1.27)
IRAS 17432−2855MC3	−8.880(0.280)	4.362(0.651)	−1.73(0.301)	−8.020(1.04)
IRAS 17432−2855MC4	46.07(1.47)	40.95(3.81)	−1.14(0.301)	−49.60(3.48)

Table 3. continued.

Source direction[a]	V_{LSR} (kms^{-1})	*FWHM* (km s^{-1})	S_{H_2CO} (Jy)	$\int S_v dv$ (Jy km s^{-1})
IRAS 17441−2822MC1	−104.2(0.390)	6.494(0.718)	−1.39(0.289)	−9.580(0.123)
IRAS 17441−2822MC2	−41.50(0.129)	4.400(0.279)	−3.79(0.289)	−17.73(0.988)
IRAS 17441−2822MC3	16.68(0.867)	40.38(1.84)	−2.38(0.289)	−102.4(4.24)
IRAS 17441−2822MC4	60.91(0.112)	28.38(0.282)	−15.0(0.289)	−454.3(4.13)
IRAS 17449−2855MC1	−4.821(0.314)	2.563(0.609)	−1.49(0.355)	−4.074(0.904)
IRAS 17449−2855MC2	14.93(0.107)	2.476(0.268)	−3.97(0.355)	−10.47(0.941)
IRAS 17455−2805MC1	−18.27(0.799)	4.990(1.91)	−1.65(0.769)	−8.769(2.82)
IRAS 17455−2805MC2	−4.021(1.17)	7.771(2.32)	−1.37(0.769)	−11.31(3.34)
IRAS 17455−2805MC3	75.90(1.60)	30.74(3.74)	−2.07(0.769)	−67.64(7.33)
IRAS 17455−2805MC4	118.6(2.38)	20.15(4.16)	−1.17(0.769)	−25.10(5.47)
IRAS 18035−2126MC1	17.52(0.236)	2.488(0.663)	−0.835(0.155)	−2.212(0.438)
IRAS 18035−2126MC2	36.30(0.179)	2.948(0.403)	−1.15(0.155)	−3.615(0.438)
IRAS 18048−2131MC1	17.82(1.16)	7.399(2.26)	−0.568(0.320)	−4.471(1.35)
IRAS 18060−2005MC1	10.32(0.190)	4.236(0.498)	−1.21(0.148)	−5.459(0.522)
IRAS 18060−2005MC2	20.55(0.433)	3.991(1.10)	−0.539(0.148)	−2.289(0.503)
IRAS 18064−2008MC1	9.857(0.424)	6.156(0.986)	−1.43(0.315)	−9.404(1.29)
IRAS 18114−1718MC1	10.71(0.398)	4.346(0.920)	−0.746(0.187)	−3.453(0.626)
IRAS 18114−1718MC2	51.34(0.276)	3.012(0.585)	−0.894(0.187)	−2.867(0.516)
IRAS 18127−1717MC1	16.52(0.711)	6.203(1.48)	−0.532(0.199)	−3.510(0.787)
IRAS 18141−1615MC1	23.76(0.402)	5.242(0.984)	−0.494(0.114)	−2.754(0.435)
IRAS 18141−1615MC2	37.28(0.339)	5.392(0.770)	−0.636(0.114)	−3.653(0.441)
IRAS 18222−1317MC1	65.56(0.294)	3.555(0.714)	−0.683(0.139)	−2.584(0.439)
IRAS 18258−0737MC1	35.80(0.519)	3.010(1.08)	−0.515(0.188)	−1.650(0.502)
IRAS 18258−0737MC2	43.14(0.293)	1.582(1.35)	−0.712(0.188)	−1.199(0.440)
IRAS 18265−1517MC1	16.89(0.477)	3.154(0.925)	−0.576(0.203)	−1.935(0.561)
IRAS 18328−0735MC1	114.0(0.199)	6.428(0.446)	−1.86(0.192)	−12.76(0.789)
IRAS 18406−0338MC1	78.72(0.690)	6.179(2.29)	−0.618(0.210)	−4.068(1.02)
IRAS 18408−0348MC1	104.1(0.857)	7.401(1.45)	−0.727(0.299)	−5.730(1.23)
IRAS 18446−0150MC1	93.78(0.299)	7.154(0.670)	−2.06(0.304)	−15.71(1.32)
IRAS 18454−0158MC1	91.88(0.151)	7.246(0.367)	−2.60(0.191)	−20.04(0.859)
IRAS 18461−0136MC1	78.21(0.721)	8.539(1.23)	−0.384(0.125)	−3.491(0.552)
IRAS 18507+0110MC1	59.67(0.129)	3.998(0.289)	−2.05(0.174)	−8.740(0.565)
IRAS 18530+0215MC1	13.72(0.202)	1.879(0.623)	−0.715(0.138)	−1.430(0.343)
IRAS 18530+0215MC2	76.87(0.619)	6.563(1.53)	−0.431(0.138)	−3.009(0.590)
IRAS 18536+0753MC1	28.79(0.333)	6.344(0.759)	−1.04(0.180)	−6.997(0.740)
IRAS 18566+0408MC1	84.70(0.373)	4.750(0.907)	−0.655(0.146)	−3.314(0.534)
IRAS 18592+0108MC1	43.20(0.147)	3.367(0.371)	−1.94(0.201)	−6.949(0.628)
IRAS 19111+1048MC1	59.94(0.616)	4.274(1.92)	−0.709(0.249)	−3.225(0.999)
IRAS 19120+1103MC1	59.29(0.135)	4.712(0.363)	−1.38(0.112)	−6.935(0.423)
IRAS 19124+1106MC1	59.30(0.566)	6.140(1.43)	−0.732(0.218)	−4.788(0.915)
IRAS 19598+3324MC1	−20.47(0.123)	3.635(0.316)	−1.10(9.359)	−4.265(0.303)
IRAS 20332+4124MC1	−3.159(0.874)	6.515(1.62)	−0.319(0.140)	−2.211(0.553)
IRAS 23033+5951MC1	−50.22(0.142)	2.899(0.309)	−0.989(0.106)	−3.051(0.292)
IRAS 23116+6111MC1	−53.13(0.437)	6.602(1.03)	−0.673(0.147)	−4.728(0.630)
G1.13−0.1 MC1	−18.69(0.367)	6.880(1.14)	−1.67(0.298)	−12.20(1.44)
G1.13−0.1 MC2	74.92(0.630)	35.01(1.45)	−2.20(0.298)	−81.99(2.90)
G10.159−0.34MC1	8.527(0.182)	11.59(0.525)	−3.00(0.200)	−36.97(1.24)
G12.807−0.20MC1	32.96(0.478)	5.638(0.114)	−7.38(0.192)	−44.32(0.769)
G15.095−0.71MC1	22.13(0.133)	1.881(0.424)	−2.04(0.233)	−4.093(0.556)
G15.181−0.63MC1	17.53(0.562)	5.844(1.40)	−1.12(0.286)	−6.960(1.23)
G19.608−0.23MC1	42.82(0.457)	6.387(1.06)	−0.776(0.183)	−5.275(0.758)
G23.421−0.21MC1	97.86(0.241)	6.340(0.434)	−1.94(0.241)	−13.08(0.930)
G30.776−0.03MC1	91.32(0.682)	6.640(0.168)	−7.13(0.247)	−50.37(1.07)
G40.505+2.54MC1	28.23(0.201)	4.934(0.557)	−1.59(0.174)	−8.352(0.704)
G48.930−0.28MC1	6.239(0.265)	1.987(0.424)	−0.509(0.115)	−1.076(0.250)
G48.930−0.28MC2	60.63(0.394)	4.306(0.792)	−0.472(0.115)	−2.162(0.377)
G49.384−0.30MC1	64.28(0.957)	6.621(0.232)	−4.39(0.211)	−30.97(0.909)
G49.582−0.38MC1	65.92(0.631)	7.953(0.157)	−8.48(0.238)	−71.75(1.15)
G79.293+1.30MC1	5.738(0.239)	3.630(0.499)	−0.458(7.488)	−1.770(0.227)
G81.253+1.12MC1	6.885(0.290)	3.695(0.663)	−0.442(8.795)	−1.737(0.276)

Notes. [a] Indicates the direction of the H_2CO molecular cloud, but we do not imply an association between the H_2CO molecular cloud and the background H II region. This table lists 59 H II regions (23 also with H110α RRLs, 36 only with H_2CO absorption lines) with H_2CO absorption lines. The values in parentheses are the formal 1σ errors of the Gaussian fit.

Table 4. Kinematic parameters.

Source	V_{LSR} (km s^{-1})	V_{TP} (km s^{-1})	D_{TP} (kpc)	D_{far} (kpc)	D_{near} (kpc)	D_{LSR} (kpc)	z (pc)	R_{GC} (kpc)	Near/Far[a]
G10.159−0.34	10.8	166.8	8.27	14.71	1.83	$1.83^{+0.79}_{-1.01}$	−11.1	6.61	N[f]
MC1	8.5	166.8	8.27	15.01	1.53	$1.53^{+0.85}_{-1.11}$	−9.3	6.90	NS[f]
G12.807−0.20	35.1	158.7	8.19	12.83	3.55	$3.55^{+0.40}_{-0.46}$	−12.6	5.00	N[f]
MC1	33.0	158.7	8.19	12.97	3.41	$3.41^{+0.41}_{-0.48}$	−12.1	5.13	NS[f]
G15.095−0.71	16.7	151.5	8.11	14.26	1.96	$1.96^{+0.56}_{-0.66}$	−24.5	6.53	N
MC1	22.1	151.5	8.11	13.82	2.40	$2.40^{+0.50}_{-0.58}$	−29.9	6.12	NS
G15.181−0.63	17.1	151.2	8.11	14.23	1.98	$1.98^{+0.55}_{-0.65}$	−21.6	6.51	N[f]
MC1	17.5	151.2	8.11	14.19	2.02	$2.02^{+0.55}_{-0.65}$	−22.0	6.47	NS[f]
G19.608−0.23	46.5	137.1	7.91	12.35	3.47	$3.47^{+0.33}_{-0.36}$	−14.2	5.26	N[f]
MC1	42.8	137.1	7.91	12.53	3.29	$3.29^{+0.34}_{-0.37}$	−13.5	5.41	NS[f]
G30.776−0.03	94.1	101.9	7.22	9.12	5.32	...	...	...	...[b,f]
MC1	91.3	101.9	7.22	9.26	5.18	...	...	...	S[b,f]
G48.930−0.28	64.5	51.9	5.52	5.52	5.52	$5.52^{+1.66}_{-1.66}$	−27.6	6.33	...[d]
MC1	6.2	51.9	5.52	10.35	0.69	$0.69^{+0.48}_{-0.49}$	−3.4	7.96	N
MC2	60.6	51.9	5.52	...	...	$5.52^{+1.66}_{-1.66}$	−27.6	6.33	S
G49.384−0.30	54.5	50.9	5.47	5.47	5.47	$5.47^{+1.64}_{-1.64}$	−29.3	6.38	...[c]
MC1	64.3	50.9	5.47	...	...	$5.47^{+1.64}_{-1.64}$	−3.7	7.97	S[c]
G49.582−0.38	59.0	50.4	5.45	5.45	5.45	$5.45^{+1.63}_{-1.63}$	−36.3	6.40	...[c]
MC1	65.9	50.4	5.45	...	...	$5.45^{+1.63}_{-1.63}$	−36.3	6.40	S[c]
G79.293+1.30	−42.0	3.9	1.56	1.56	1.56	$1.56^{+0.47}_{-0.47}$	35.3	8.25	...[d]
MC1	5.7	3.9	1.56	1.56	1.56	$1.56^{+0.47}_{-0.47}$	35.3	8.25	...[c]
G81.253+1.12	12.7	2.7	1.28	1.28	1.28	$1.28^{+0.38}_{-0.38}$	25.1	8.30	...[c]
MC1	6.9	2.7	1.28	1.28	1.28	$1.28^{+0.38}_{-0.38}$	25.1	8.30	...[c]
IRAS 06053−0622	10.2	...	...	0.74	0.74	$0.74^{+0.63}_{-0.57}$	−161.4	9.01	...[e]
MC1	10.5	...	...	0.77	0.77	$0.77^{+0.63}_{-0.57}$	−168.0	9.03	...[e]
IRAS 18060−2005	7.8	166.3	8.26	15.12	1.41	$15.12^{+1.13}_{-0.87}$	−39.6	7.02	F[f]
MC1	10.3	166.3	8.26	14.78	1.75	$14.78^{+1.02}_{-0.79}$	−38.7	6.69	FS[f]
MC2	20.6	166.3	8.26	13.68	2.85	...	...	...	...[d,f]
IRAS 18141−1615	33.8	153.1	8.13	13.02	3.24	$3.24^{+0.40}_{-0.46}$	0.7	5.33	N
MC1	23.8	153.1	8.13	13.69	1.75	$1.75^{+0.49}_{-0.57}$	0.4	6.72	N
MC2	37.3	153.1	8.13	12.81	2.85	$2.85^{+0.38}_{-0.43}$	0.6	5.69	NS
IRAS 18222−1317	48.8	141.8	7.98	12.27	3.70	$12.27^{+0.35}_{-0.32}$	−62.1	5.02	F[f]
MC1	65.6	141.8	7.98	12.86	3.11	...	...	...	...[d,f]
IRAS 18454−0158	99.0	101.8	7.21	8.83	5.60	...	...	...	...[b]
MC1	91.9	101.8	7.21	10.48	3.94	...	...	...	S[b]
IRAS 18507+0101	54.7	91.5	6.94	10.46	3.43	$3.43^{+0.36}_{-0.36}$	9.2	5.89	N
MC1	59.7	91.5	6.94	8.36	5.53	$5.53^{+0.65}_{-0.47}$	14.8	4.93	NS
IRAS 18592+0108	45.6	88.7	6.86	10.76	2.97	$2.97^{+0.37}_{-0.38}$	−90.4	6.21	N
MC1	43.2	88.7	6.86	10.02	3.71	$3.71^{+0.37}_{-0.37}$	−113.0	5.78	NS
IRAS 19120+1103	56.1	60.5	5.89	7.61	4.17	...	...	...	...[b,f]
MC1	59.3	60.5	5.89	8.67	3.12	...	...	...	S[b,f]
IRAS 19598+3324	−23.3	12.6	2.83	2.83	2.83	$2.83^{+0.85}_{-0.85}$	79.0	7.91	...[c]
MC1	−20.5	12.6	2.83	2.83	2.83	$2.83^{+0.85}_{-0.85}$	79.0	7.91	...[c]
IRAS 23116+6111	−59.3	...	...	4.86	4.86	$4.86^{+0.67}_{-0.64}$	65.9	11.1	...[e]
MC1	−20.5	...	...	1.48	1.48	$1.48^{+0.60}_{-0.62}$	20.1	9.05	...[e]

Notes. [a] (N) A source at the near kinematic distance; (F) a source at the far distance; (S) a molecular cloud associated with an H II region; (NS and FS) a molecular cloud associated with an H II region at the near and far distance, respectively. [b] No classification or distance is given for this source; [c] this source is located at the tangent point; [d] the distance ambiguity cannot be resolved; [e] this source is located in the outer Galaxy; [f] Downes et al. (1980) have reported this source's kinematic distance.

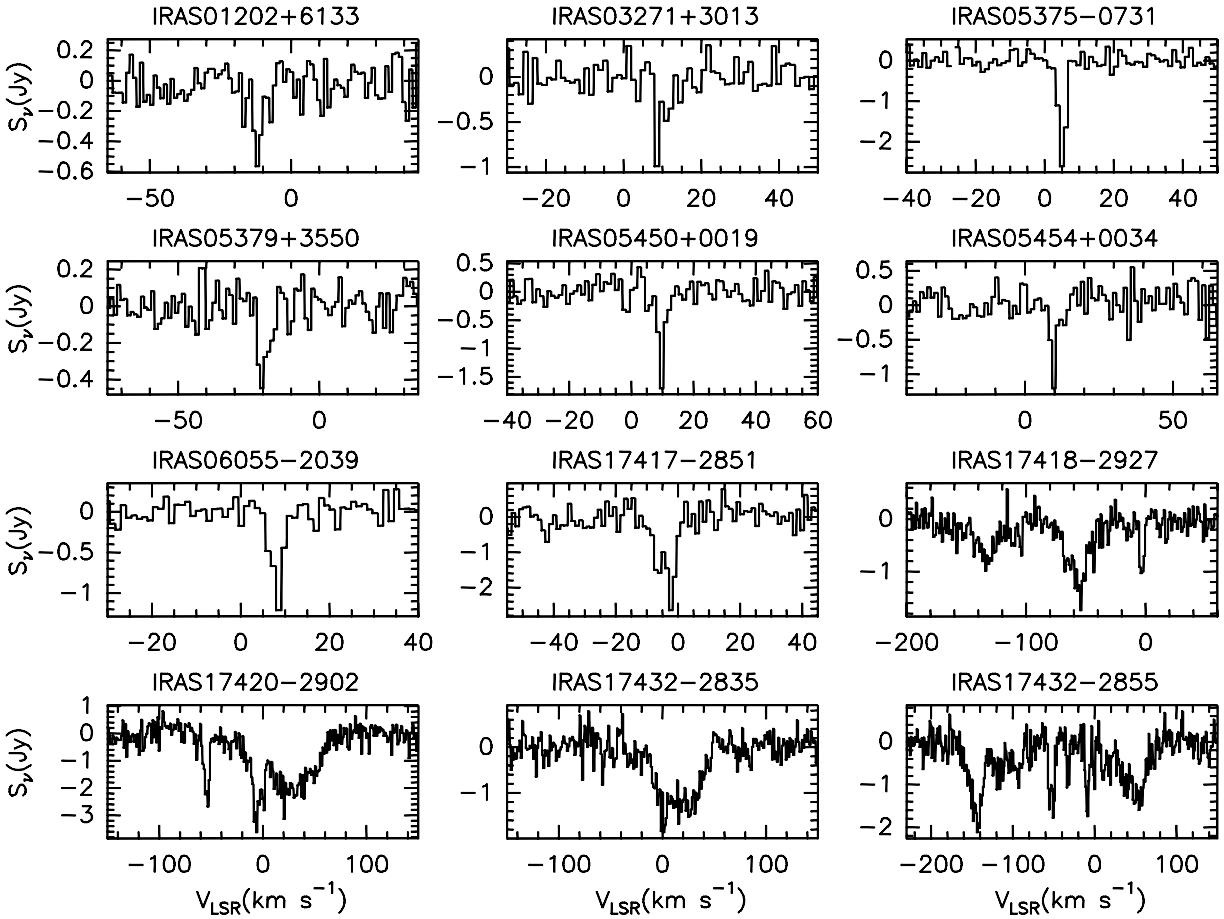

Fig. 1. H_2CO absorption lines observed toward 36 H II regions, the source name is given at the top of each panel.

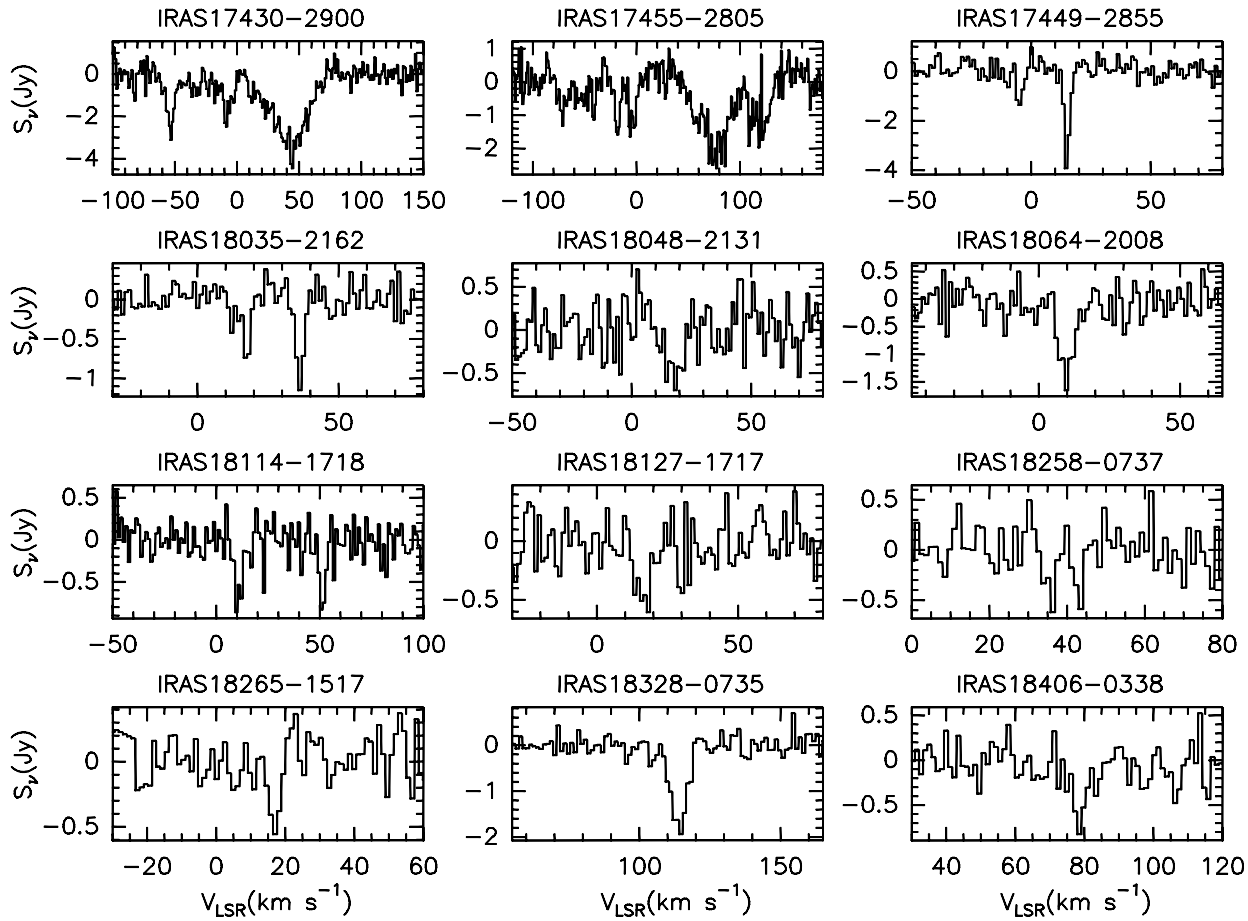

Fig. 1. continued.

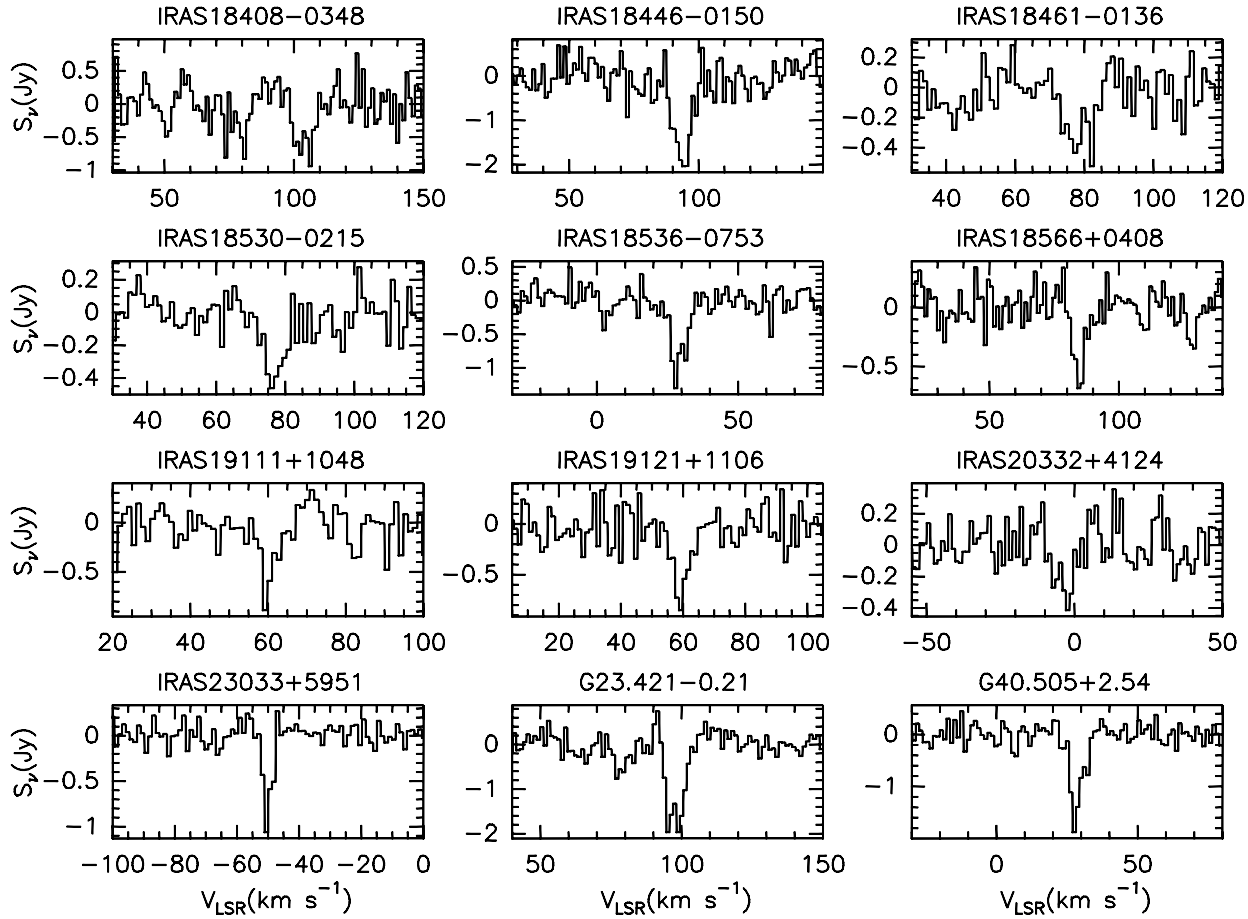

Fig. 1. continued.

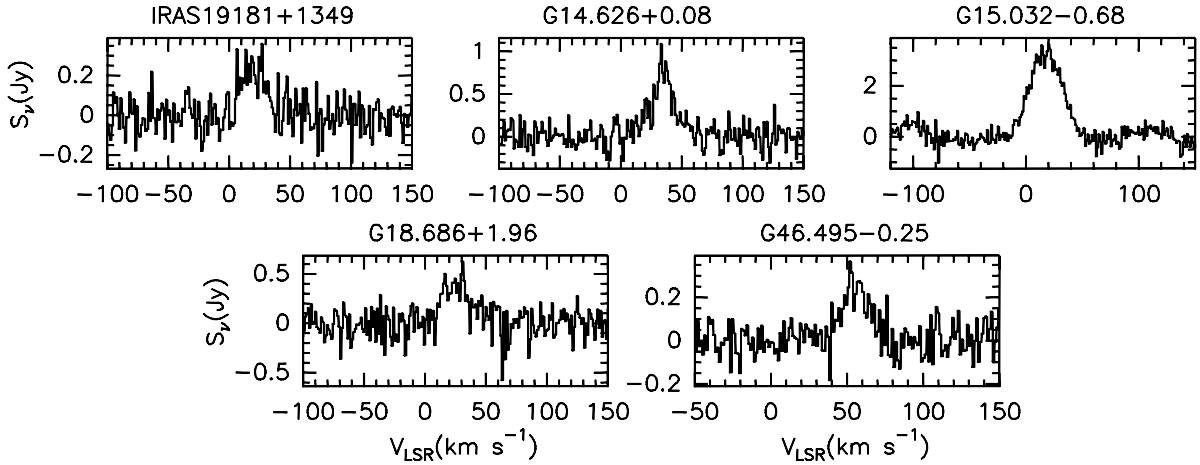

Fig. 2. H110α RRLs observed toward five H II regions, the source name is given at the top of each panel.

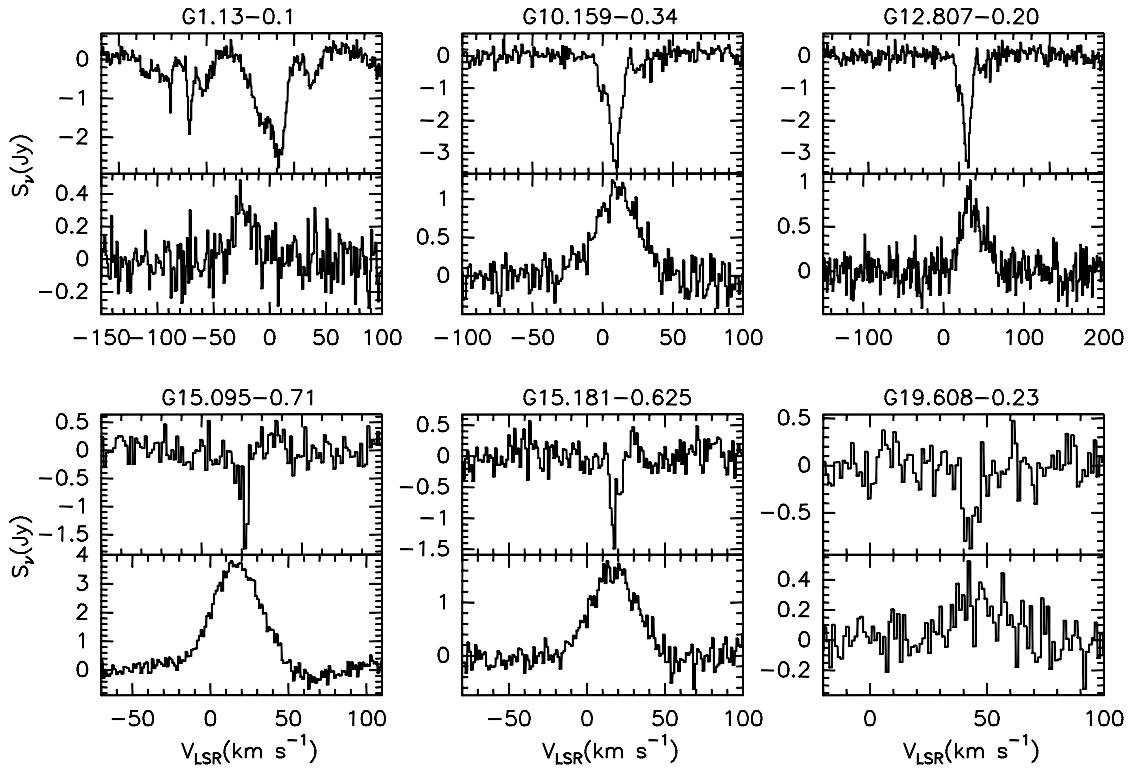

Fig. 3. Spectra of H_2CO absorption lines (*upper panel*) and H110α RRLs (*lower panel*) observed toward 23 H II regions. The source name is given at the top of each panel.

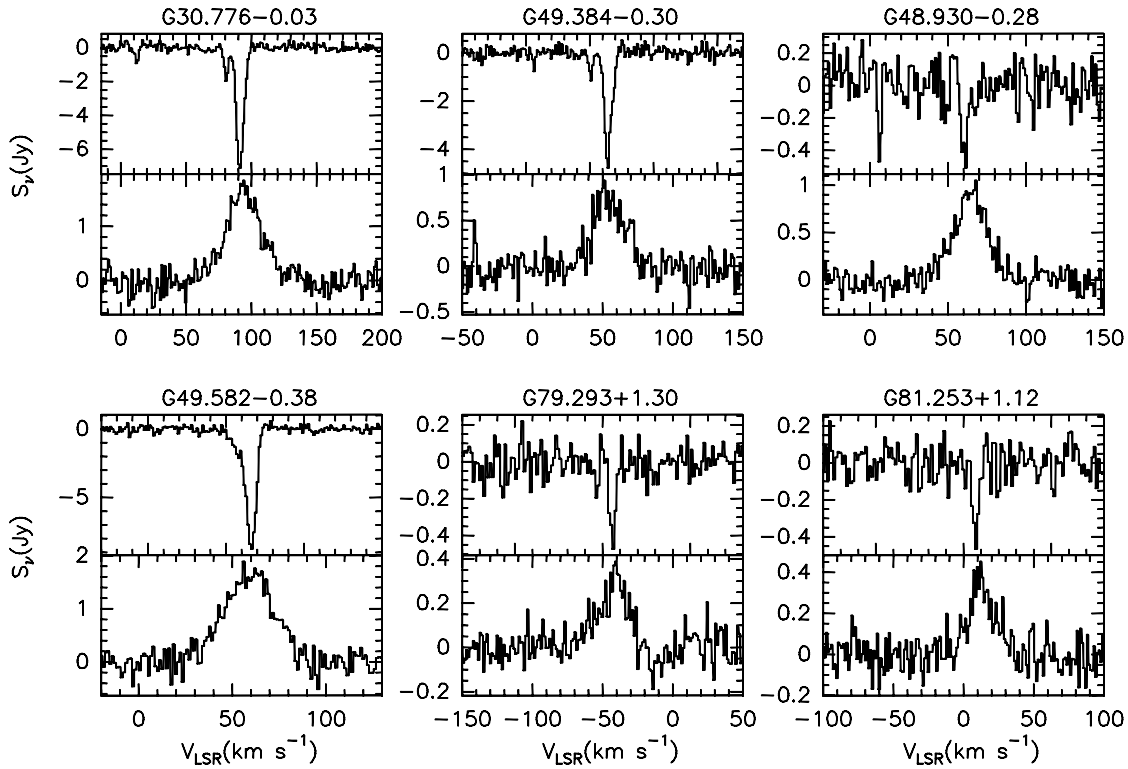

Fig. 3. continued.

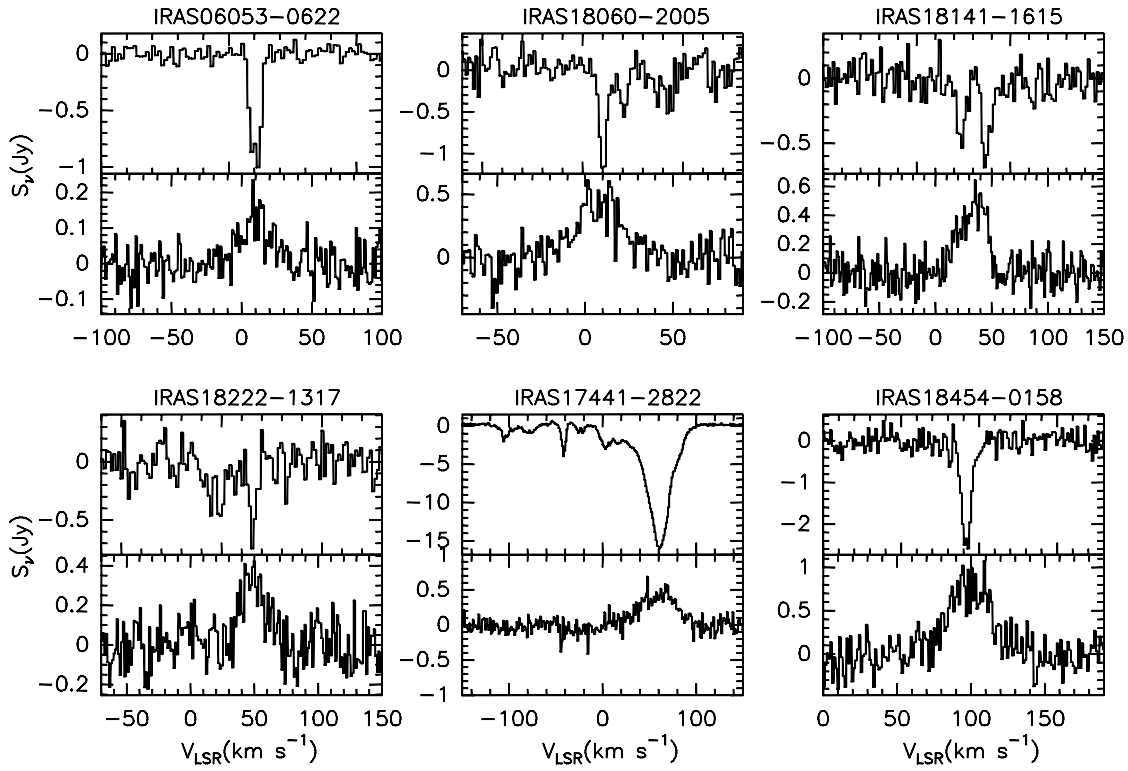

Fig. 3. continued.

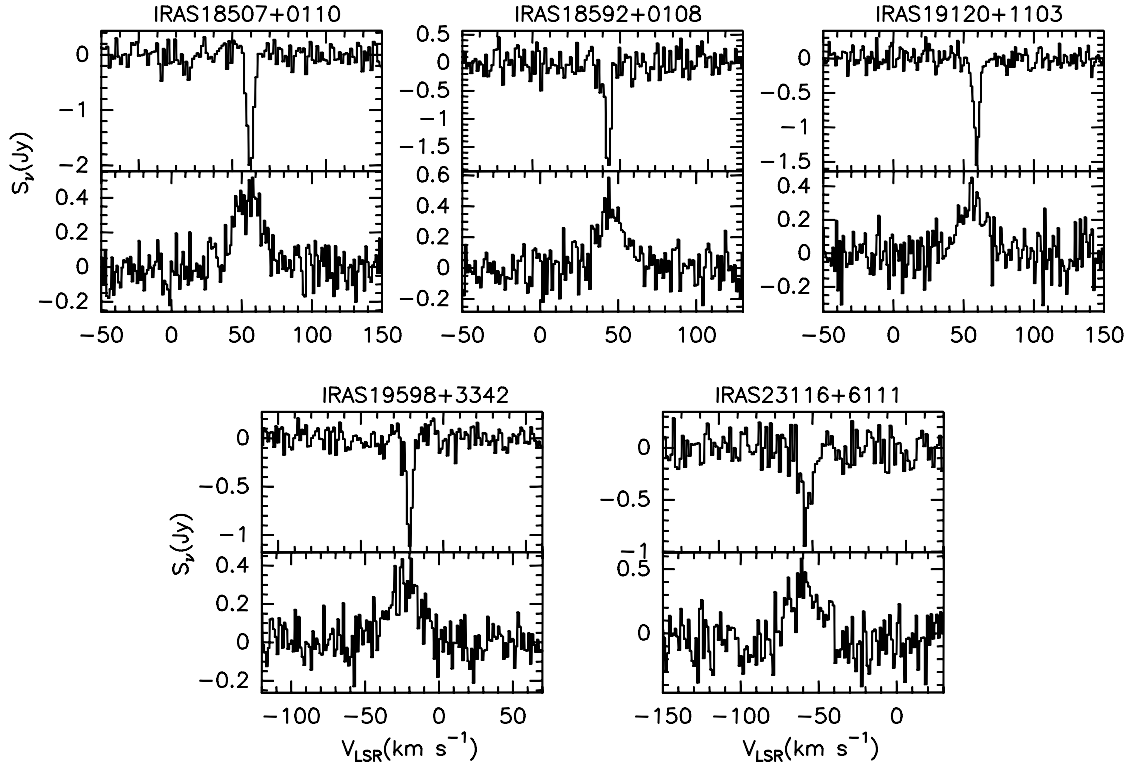

Fig. 3. continued.